PAPER • **OPEN ACCESS**

A wavefront track approach to defect detection in composites by scanning laser Doppler vibrometry

A wavefront track approach to defect detection in composites by scanning laser Doppler vibrometry

D Candelaresi[1], A Annessi[2], G Allevi[1], M Martarelli[1] and P Castellini[1]

[1] Department of Industrial Engineering and Mathematical Sciences, Università Politecnica delle Marche, v. Brecce Bianche 11, Ancona 60131, Italy
[2] Department of Agricultural, Food and Environmental Sciences, Università Politecnica delle Marche, v. Brecce Bianche 11, Ancona 60131, Italy

e-mail: d.candelaresi@pm.univpm.it, 0009-0008-4191-3400

Abstract. Composite laminates are becoming increasingly popular in a large variety of applications due to their favourable mechanical properties. However, laminates production processes can lead to various defects in the final material. The most common type is related to thickness variations, e.g. delaminations between layers, which can compromise the mechanical strength of the structure. Therefore, there is a great interest in developing non-destructive and non-contact quality control techniques for composite material assessment to minimize process costs. An interesting approach is the use of laser Doppler vibrometry combined with signal analysis based on Lamb waves propagation. In this work, we used an impulsive force given by a piezoelectric disk to the specimen and a laser Doppler vibrometer acquiring the points velocity over time along a scanning grid on the surface. The specimen is a fiberglass reinforced flat panel with seven different orientated layers which presents a delamination of about 22 mm. The maximum thickness-frequency product achieved in this analysis has been 0.2 MHz·mm. In contrast to state-of-the-art methods for identifying thickness variation based on local estimation of the principal wave number, the proposed algorithm makes use of a tracking filter of the wave front of the propagating A0 mode waves, returning a final image in polar coordinates. The final information given by the algorithm provides the position of the delamination and, hence, can be used as a pass/failure test. State-of-the-art methods are also able to identify the shape of the defect but pay the price of a higher computational cost by using at least 4D matrix processing unlike our method which only uses 3D matrices.

1. Introduction

Nowadays, the use of composite materials is widespread over a multitude of engineering application fields ranging from aerospace, automotive, marine, energy to biomedical [1]–[3] due to their high strength-to-weight ratio, high-fatigue resistance and corrosion resistance [4]. Composite production is a special addictive process as the material and final product are manufactured simultaneously. The product quality is affected by process parameters variations and human factors, due to the need of human operators. This uncertainty in the production can result in a wide range of defects, such as delamination and debonding [5]. Their assessment is crucial when dealing with composite structures due to the structural performance reduction related to their presence. Therefore, it is important to rely on robust and well-established non-destructive testing techniques [6]. Today's quality control technologies aim to be non-destructive and based on non-contact method to achieve process versatility and reduce inspection

time and related costs. Structures made by composite materials are laminates consisting of several layers whose thickness is much smaller than other dimensions and, therefore, can be considered thin. In this case, it is known that propagating elastic waves have a wavelength dependent on the product frequency times thickness [7]. Lamb waves are guided: only two propagation modes originate at zero frequency and remain present throughout the spectrum ("antysimmetric" A0 and "symmetric" S0 modes) [8] but there is an infinite number of dispersive modes which appear at gradually increasing frequencies [9]. Guided waves are characterized by a lower attenuation if compared to bulk waves in solid-walled components. Both assumptions are useful to simplify signal analysis making possible to isolate the main propagation mode and observe the effect of the defect in its dispersion curve. In addition, with a single excitation point, Lamb waves can cover long distances with a good signal-to-noise ratio [10]. Considering delaminations the most critical and common type of defects [11], these features make the propagation of Lamb waves the foundation of the current non-destructive testing (NDT) techniques based on laser vibrometry. Standard ultrasonic probes need to be in contact with the surface under test or use of a coupling medium. On the contrary, Scanning laser Doppler vibrometry has the advantage of being non-contact. Over the years, various techniques for Lamb wave analysis have been proposed, which can be divided into two groups. The former techniques are based on time history signal (e.g points velocity on time) and extract features like Time of Flight (ToF). It is generally defined as the time lag between time instant of actuator response to excite a guided wave and the first wave packet captured by a sensor [12]. The use of ToF can be a straightforward method for damage detection using triangulation [13]. Other similar approaches make use of Wavelet Transform (WT) [14,15] to find discontinuities originating from the presence of delamination on time domain. Moreover, Artificial Neural Networks (ANN) have been applied to damage identification (e.g Zang et al. [16]). However, except for a few successful applications in the localization of the damage, direct time-series analysis is in general unable to isolate appropriately scattered information due to the presence of a defect from noise even if considering different frequency bands [17].

The latter methods are based on image processing and rely on dispersion diagram to highlight faults. In fact, a variation in thickness due to the presence of a discontinuity in the material is related to a change in the wavenumber of propagating Lamb waves, which can be exploited to localize the defect.

A method referred as Spatial Wavenumber Imaging (SWI) identifies the defect through a wavenumber colormap with the coordinates of the acquisition points as axes. In each acquisition point a spatial window is set on which the 3D Fourier Transform is applied. The transform accounts for three dimension, two dimensions regard spatial coordinates and the other regards the time one. The final image is built plotting the wavenumber corresponding to maximum amplitude spectrum summing each frequency [18]. The main limitation of this technique is related to the resolution of the defect. In fact, its localization depends on the size of the window: the larger it is, a more resolved shape will be at the expense of the localization. Therefore, it is mandatory to choose the best window size for the specific situation. 2D Continuous Wavelet Transform can be introduced to improve the previous method, replacing wavenumbers with scales [19]. In this case, since the transform is continuous, there is no need to define a spatial window but, on the other side, the computational load increase due to the addition of at least scale axis as new dimension. A different approach was taken by Spytek at el. [20] and Flynn at el. [21], which divided the wavenumber range into subbands instead of using windows to divide the acquisition spatial domain. However, the final image where the defect can be highlighted is still a wavenumber colourmap. Furthermore, the introduction of subbands raised the dimensionality of the original problem. When dealing with flat panels, A0 mode is the more easily excited and carries most of the energy [22]. For this reason state-of-the-art methods reported in [20]-[21] are based on the separation of Lamb's wave propagation modes following A0 dispersion curve.

In this paper, we present a method based on tracking the wavefront related to the main A0 mode propagating over time at its phase velocity.

Piezoelectric elements (PZTs) are widely used as transducers and actuators for fault detection. They have been proved to be stable and effective for Lamb wave generation [23]. For our application, Lamb waves were generated using a piezoelectric disk actuator glued on a flat panel made of seven layers of

fiberglass reinforced plastic. Velocity signals are acquired on the opposite side with respect to the excitation using a Scanning Laser Doppler Vibrometer (SLDV) along an equally spaced points grid. The method consists of three steps. In the first part, the dispersion diagram of the material is empirically derived. In the second step, the phase velocity is retrieved by means of the A0 mode in the experimental dispersion curve. Lastly, the wavefront of the isolated A0 mode is tracked during propagation over each time instant using a circle as wave estimation, starting at the source as a point and expanding at the propagation speed of the material. The final plot, in which the defect is highlighted, is obtained as the stack of velocity values along the arc of the circle at each time instant (which is related to radius through propagation speed). The plot has the angular and radial position of the wavefront tracking circumference respectively on *x*- and *y*-axis. Like all the previous methods, the proposed one is limited to area-spanning defects whose size is greater than the spatial resolution used in the scanning grid.

The paper is organized as follows: the first section describes the specimen and the setup used in the experiments; in the second section, we discuss the processing algorithm broken down into the steps; finally, the results are given along with future development of the proposed method.

2. Specimen and detection setup

The method proposed by the authors was applied to a Fiberglass Reinforced Plastic (FRP) flat panel (0.200 m × 0.200 m × 0. 002 m) wherein a defect was specifically produced in order to simulate faulty bonding conditions and thus emulating a delamination. The panel is made by a stack of seven plies. Damage was simulated by including a wax disk (diameter of about 0.022 m) at different depths with respect to the ply that would have been chosen as the measurement side, as depicted in Figure 1.

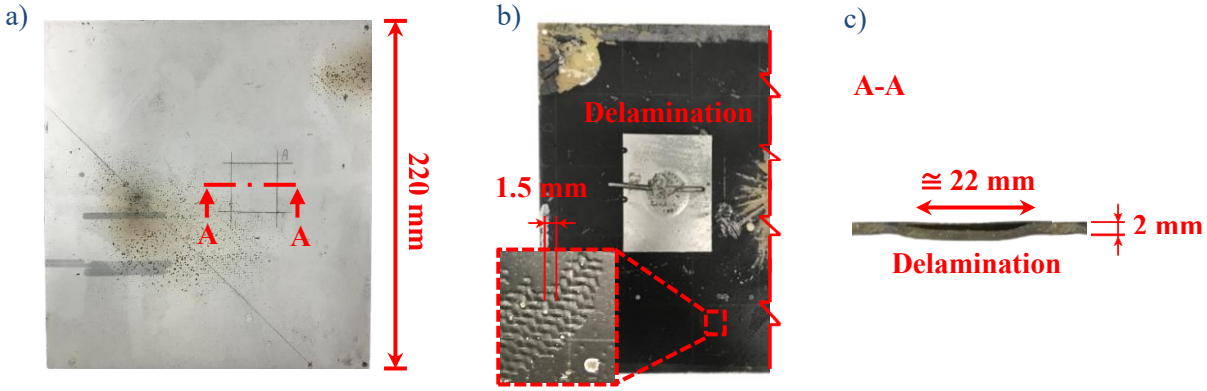

Figure 1. Specimen used with an enlargement highlighting the diameter of the fiberglass: a) rear view; b) front view (measurement surface); c) cross section A-A (using a similar defect for the photo)

The experimental setup used is shown in Figure 2. The panel was tested in almost free-free condition to maintain boundary conditions as close as possible to the ones found in the literature for the determination of dispersion diagrams. For this reason, the specimen was placed on a foam support. The scanning laser Doppler vibrometer (sLDV) measures out-of-plane velocity response over time on each point of the measurement grid. Acquisition parameters are reported in

Table **1**. The excitation is given by means of a piezoelectric disk, with a diameter equal to 10 mm, installed using HBM X60 glue on the opposite surface with respect to the one scanned with the vibrometer. The pulse generator is triggered by the vibrometer controller to synchronize measurements. Initially, a preliminary measurement campaign is carried on to extract dispersion curves, which are required to estimate the main propagation mode and thus the phase velocity of the main wave, strongly dependent on material properties. In this case, the actuator was fed with a sine step excitation signal with frequency reported in Table 2. The acquisition was conducted along a line passing through the center of the piezoelectric disk consisting of 134 equally spaced points with a spatial resolution of 1.9

mm. Thereafter, in the case of point grid measurement, the piezoelectric disk receives an impulse as excitation signal for each measurement acquired. The use of an impulsive signal allows to obtain a broadband excitation, in the frequency band of interest spanning from 0 Hz to 100 kHz. This approach is needed since the frequency range in which the defect will have an influence is not known in advance. The maximum characteristic thickness-frequency product achieved in this work has been 0.2 MHz·mm.

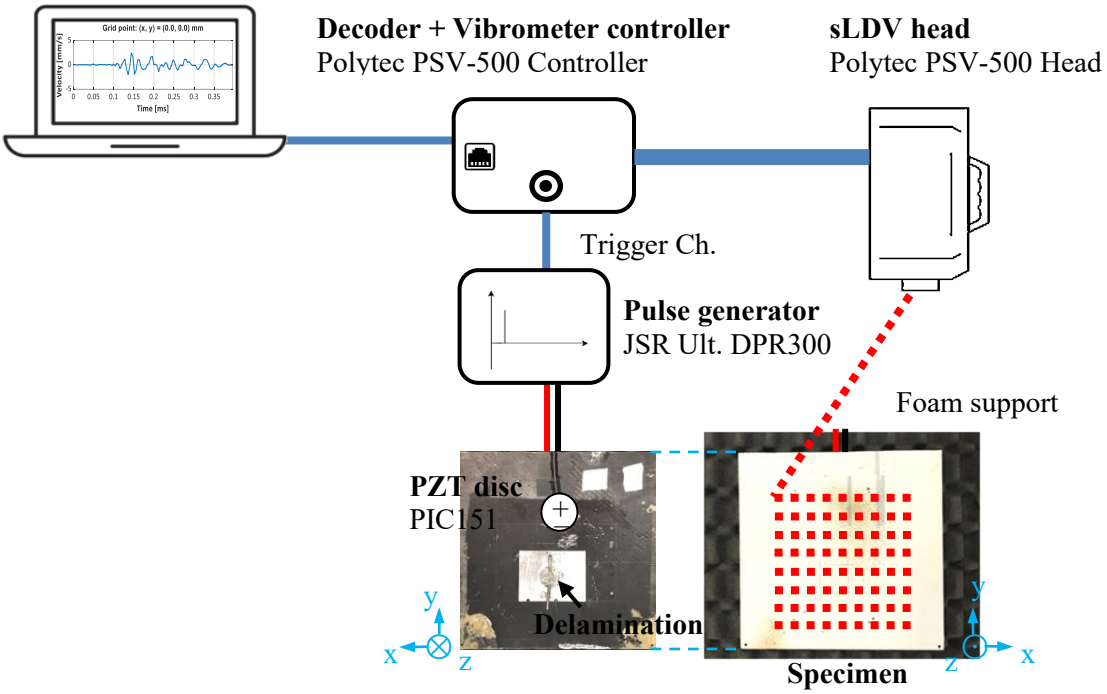

Figure 2. Experimental setup for defect detection.

Table 1. Data acquisition parameters

Measurement mode	Trigger on generator waveform
Averaging quantity	Velocity time signal [mm/s]
Averaging mode	linear
Averaging count	16
Sample period	20 ms
Sample frequency	250 kHz
Vibrometer direction	+ Z
Range	[-20; 20] mm/s
A/D converter bit number	32
Bandwidth	[0; 100] kHz
Tracking filter	On (Fast)

Table 2. Excitation waveforms parameters used in the two test phases

Scanning grid	Spatial resolution	Generated signal	Bandwidth
134 points line	≅1.9 mm	Sine step	{1, 10, 25, 35, 45, 50, 55, 65, 70, 75, 85, 95} kHz
67 × 67 points	≅1.9 mm	Impulse	[0; 35] MHz

3. Method for defect detection

The method proposed for defect detection consists of four steps defined in the flow chart of Figure 3:

1) Determination of the dispersion curve corresponding to the principal wave propagation mode.
2) Estimation of phase velocity of the main mode.
3) Tracking of the principal propagating mode on velocity data using an arc of circumference expanding at the estimated phase velocity as wavefront.
4) Removal of the effects given by the anisotropy of the material.

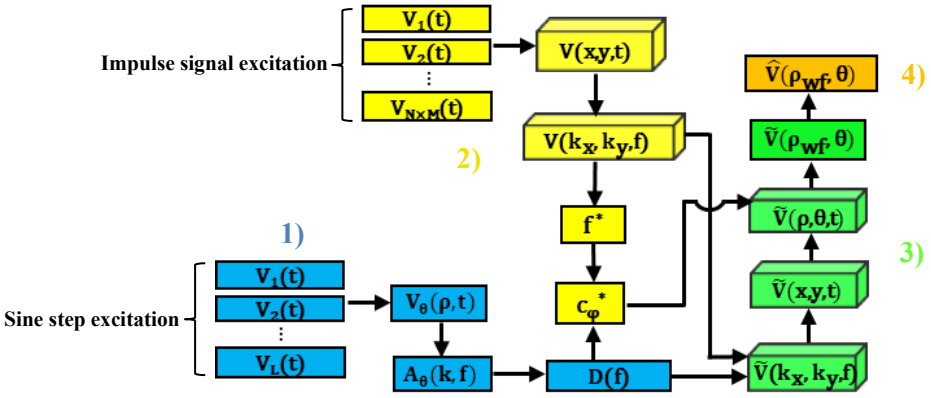

Figure 3. Signal processing flowchart. The steps of the proposed method are highlighted in colours.

3.1 Dispersion curve determination for the A0 mode

According to Su et al. [17], pure sinusoidal waveforms appear to excite Lamb wave harmonics more efficiently than other type of signals since they concentrate energy in a narrower spectrum. To characterise the dispersion diagram and extract the main propagation mode, the set of pure sinusoid frequencies specified in Table 2 as been used. In this step, velocity $V_i(t)$ (mm/s) was acquired by SLDV along a line path of 134 points (i stands for point index, t for time instant) with a spatial resolution of approximately 1.9 mm. The line passes through the centre of the piezoelectric disk to investigate the radial direction exiting from the source, which can be considered as point-like. The line considered was chosen in order to have the greatest number of measurement points to increase wavenumber resolution. Although the specimen is an anisotropic medium, the dispersion diagram calculated on this line does not deviate from the mean diagram evaluated in all directions, as it is shown below. For the notation, a polar coordinate system is used where θ is the angle while ρ is the radius, as depicted in Figure 4b. The acquired velocities $V_i(t)$ were arranged in the matrix $V_\theta(\rho, t)$ (mm/s) where the subscript θ (°) indicates that points does not vary in the angular direction and therefore are aligned, while ρ (mm) indicates the distance from the centre of piezoelectric disk, which corresponds with the origin of the polar coordinate system. The modulus of the 2D Fourier Transform is used to estimate the dispersion

curves in the plate, obtaining the matrix $A_\theta(k,f)$ where k (mm^{-1}) is the wavenumber along propagating direction θ and f (kHz) is the frequency:

$$A_\theta(k,f) = |\mathrm{fft2}\{V_\theta(\rho,t)\}| \tag{1}$$

The dispersion diagram obtained is weakly influenced by the propagation direction chosen for the estimation of dispersion curves of the main mode, i.e. the orientation along θ. To justify that the chosen line does not greatly influence the characterization of the dispersion curve of the main mode, the dispersion diagram of the medium was also evaluated from the acquisitions made with the impulse signal provided to piezoelectric disc.

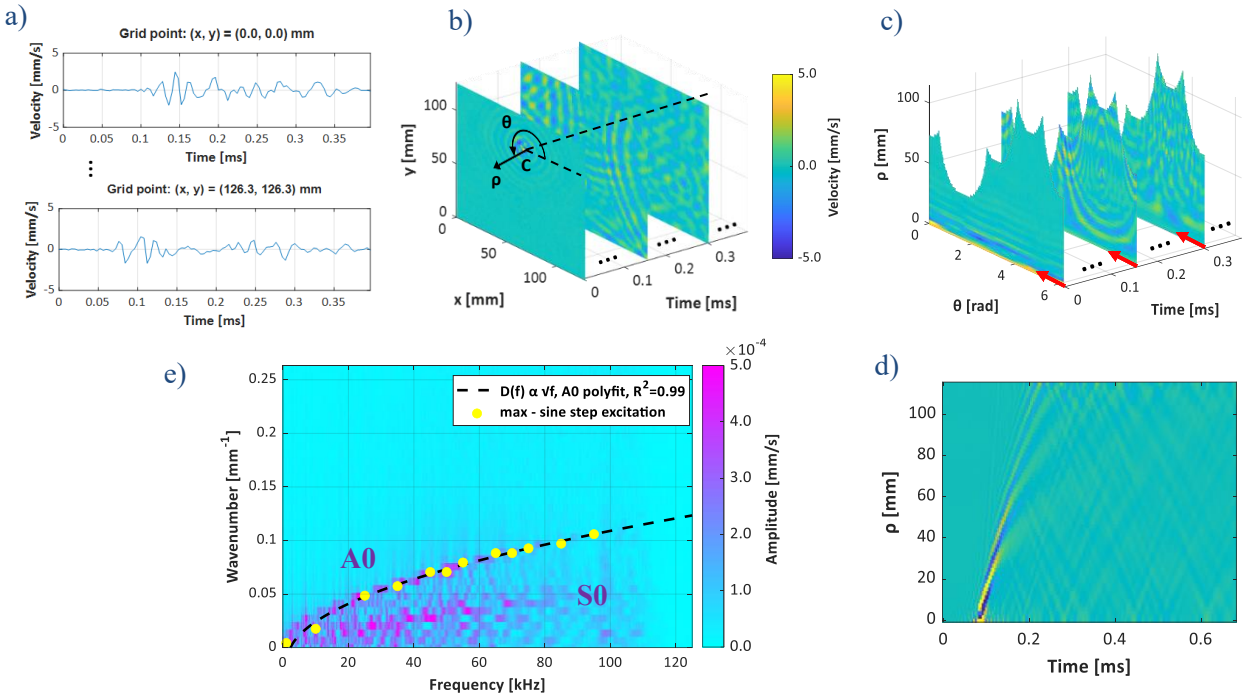

Figure 4. a) Measured points velocities time histories $V_i(t)$; b)Velocity matrix in Cartesian coordinates $V(x,y,t)$ along with the schematics of the polar transformation; c) Velocity matrix in polar coordinates $V(\rho,\theta,t)$; d) $\bar{V}_\theta(\rho,t)$; e) $\bar{A}_\theta(k,f)$ and superposition of the points of spectral maxima with sine step excitation with a polynomial curve $D(f)$ of order ½ to fit mode A0.

Velocity signals $V_i(t)$ were acquired on a $N \times M = 67 \times 67$ scanning point grid and arranged in a matrix form $V(x,y,t)$. A polar coordinate transformation with origin at the piezoelectric disk centre was applied to the matrix of acquired data obtaining $V(\rho,\theta,t)$. The polar coordinate transformation preserves the spatial resolution of 1.9 mm used in the cartesian grid making use of a linear interpolation. In order to consider all the propagation directions, $V(\rho,\theta,t)$ was averaged over all angles θ obtaining $\bar{V}_\theta(\rho,t)$ and then calculated $\bar{A}_\theta(k,f)$ following equation (1). The cartesian to polar coordinate transformation is given by equation (2):

$$\begin{cases} x = \rho\cos\theta + x_0 \\ y = \rho\sin\theta + y_0 \end{cases} \tag{2}$$

where $C = (x_0; y_0)$ corresponds to the center of the piezoelectric disk.

The two zero-frequency modes appear in the dispersion diagram of Figure 4e. The A0 mode carries most of the energy and therefore has the best signal-to-noise ratio as well as being the one highlighted with sine step excitation. A polynomial $D(f)$ of order ½ can be used to fit sine step data points in the dispersion diagram. In fact, for thickness-frequency product range of interest, phase velocity c_φ (m/s) is given by equation (3):

$$c_\varphi = \frac{f}{k} \tag{3}$$

c_φ is proportional to the square root of the frequency [24] as well as the wavenumber k .This is confirmed also by the high value of the coefficient of determination $R^2 = 0.99$ found.

As clearly shown in Figure 4e, point data obtained with sine step excitation (highlighted in yellow) are overlapped with the maximum amplitude (highlighted in fuchsia) of the dispersion plot obtained from the averaged polar velocity $\overline{V}_\theta(\rho,t)$ in the case of impulsive excitation. Although $D(f)$ has been evaluated considering only a single direction of propagation, it can describe the propagation mode A0 along all propagation directions in the specimen.

3.2 Phase velocity estimation of the main A0 mode

Once the dispersion relation for the A0 mode $D(f)$ is estimated, the phase velocity can be computed for the propagating mode, which is the one characterized by most of the energy. The first step is to calculate the amplitude spectrum of $V(x,y,t)$ using the 3D Fourier transform:

$$V(k_x,k_y,f) = \mathrm{fft3}\{V(x,y,t)\} \tag{4}$$

where k_x, k_y (mm^{-1}) are the projection of wavenumber along *x* and *y* direction. Thereafter, $A(k_x,k_y,f)$ is computed as the amplitude of the spectrum $V(k_x,k_y,f)$.

To select the frequency f^*, characterized by the bigger energy content in the spectrum, the maximum of A has been chosen, as depicted in Figure 5b. Once the dispersion relation $D(f)$ is known, the phase velocity $c_\varphi{}^*$ of mode A0 is calculated through equation (5), as graphically shown in Figure 5c:

$$c_\varphi{}^* = \frac{f^*}{D(f^*)} \tag{5}$$

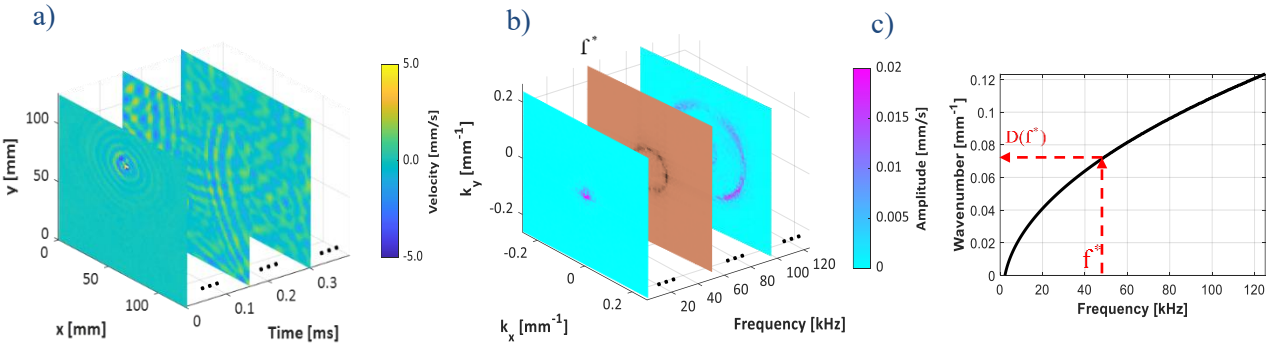

Figure 5. Estimation of main phase velocity: a) Velocity matrix $V(x,y,t)$; b) Amplitude matrix of the 3D spectrum along $A(k_x,k_y,f)$ with frequency f^*, corresponding to the maximum amplitude; c) A0 dispersion fitting curve $D(f)$ and graphical determination of phase velocity.

3.3 Wavefront tracking in the spatial domain

The calculated phase velocity may not be unique due to the presence of the S0 mode whose dispersion curve may have the same slope as $D(f)$ at another frequency value. To avoid this and follow a single wavefront, the A0 mode can be isolated by filtering all the rest of the dispersion diagram since its analytical expression is known. A Gaussian bandpass filter $G(k_x, k_y, f)$, shown in Figure 6, with standard deviation $\sigma(f)$ and mean $D(f)$ has been applied to $V(k_x, k_y, f)$ (see equation (6)):

$$G(k_x, k_y, f) = e^{-\left(\frac{k_x^2 + k_y^2 - D(f)^2}{\sqrt{k_x^2 + k_y^2}\cdot\sigma(f)}\right)^2} \tag{6}$$

where $\sigma(f) = \alpha \cdot D(f)$ with α a real constant. When the product between frequency and thickness in near to zero, the A0 and S0 mode dispersion curves are very close whilst they diverge as the frequency increases. However, as the frequency increases, the experimental A0 dispersion curve diverges from the parabolic fitting curve $D(f)$. Therefore, $\sigma(f)$ needs to increase over frequency.

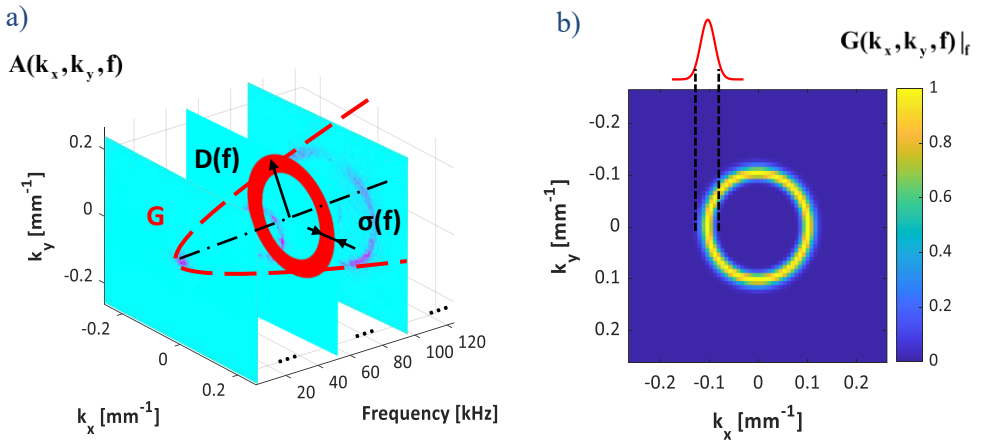

Figure 6. Gaussian bandpass filter: a) filter application domain on $A(k_x, k_y, f)$; b) filter support representation for a selected frequency f.

The simplest expression suitable for $\sigma(f)$ is a linear one. The purpose of introduce parameter α is hence to separate A0 dispersion curve represented by $D(f)$ from the mode S0. For this reason α can't be set to a value much higher otherwise mode S0 curve will not filtered. On the other hand the parameter α should not be set at a value close to zero to avoid too narrow bandpass and thus an image corrupted by ringing, as a result of the inverse transform is performed in the next step. A reasonable value is $\alpha = 25\%$. Lastly, to get the wavefront tracking, it is necessary to return to the time domain through the inverse transform (see equation (7)):

$$\tilde{V}(x, y, t) = \text{fft3}^{-1}\{V(k_x, k_y, f) \cdot G(k_x, k_y, f)\} \tag{7}$$

where $\tilde{V}(x, y, t)$ (mm/s) is the velocity matrix belonging to the A0 mode wave propagation.

The tracking of the A0 mode wavefront moving at c_φ^* is done using a circumference centred on the piezoelectric actuator, which increase its radius at the wave speed. The polar transformation introduced earlier is still needed to change the cartesian coordinate to $\tilde{V}(\rho, \theta, t)$ (see equation (2)). The radius of

wavefront tracking circumference ρ_{wf} (mm) increase with the simple law of wavefront propagation given by equation (8):

$$\rho_{wf}(t) = c_{\varphi}^{*} \cdot (t - t_0) \tag{8}$$

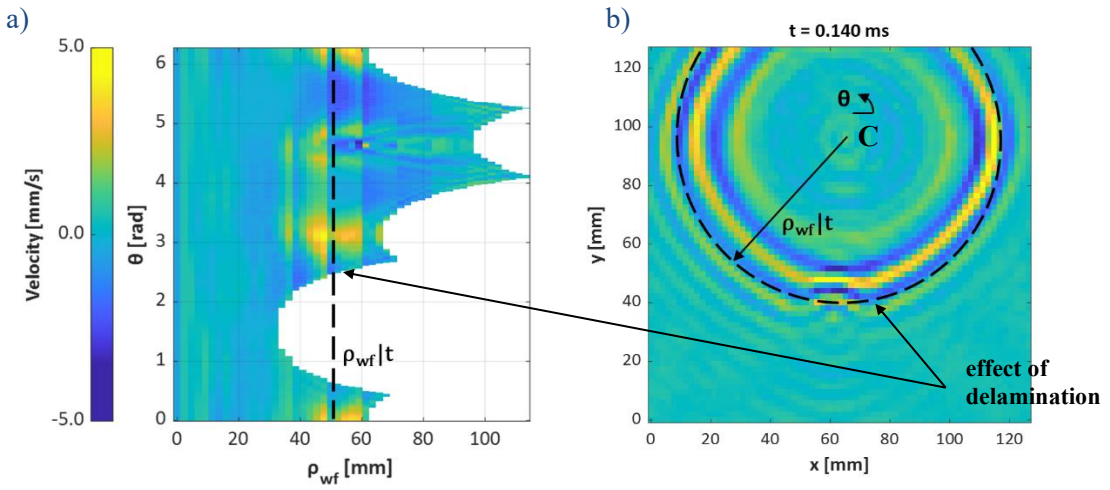

Figure 7. Plots of the circumference based wavefront tracking from the centre of piezoelectric disk: a) $\tilde{V}(\rho_{wf}, \theta, t)$; b) $\tilde{V}(x, y, t)$

where t_0 (ms) is the pre-trigger duration. For each time instant t, $\tilde{V}(\rho_{wf}(t), \theta)$ has been evaluated, as shown in Figure 7. It represents the positions of the main wavefront over the entire time history and, therefore, the circle radius. When a surface wavefront propagates above the delamination its phase velocity changes due to material thinning and instantaneous velocity values captured by circumference tracking differ. Delamination effect is visible for $\rho_{wf} \cong 50$ mm for $\theta \cong 4.5$ rad in Figure 7. Delamination also causes diffraction of the elastic waves and this can be seen as the points velocity are in phase in a non radial direction over the defect.

3.4 Removal of the effects of material anisotropy

Although the defect is visible, velocity amplitudes along the circumference are not uniform, even far from the delamination. If the dispersion curves can be assumed to be approximately equal, this does not imply that differences in wavefront displacement at various angles can be neglected because they accumulate over time. Strictly speaking, tracking the wavefront with a circumference would only be accurate for an isotropic medium. Therefore, a high pass filter [25] with cutting frequency f_c is applied along θ to attenuate variations in the image due to non-isotropic wave propagation. Cutting frequency can be set through equation (9):

$$f_c(\rho_{wf}) = \frac{D_{def}^{max}}{2\pi \cdot \rho_{wf}} \tag{9}$$

where $\Delta\theta$ (rad) is the angular resolution used in equation (2) to preserve spatial resolution and D_{def}^{max} (mm) is the maximum expected size of defects, here set to 25 mm. After polar transformation, defect sizes appear proportional to radial position ρ_{wf} of the expanding circumference and, thus, also the cut-off frequency f_c. The filter is a high pass type because the velocity variations due to anisotropy contribute

at lower frequencies with respect to those produced by the wavefronts interacting with the defect. The filtered final image, showing the matrix $\hat{V}(\rho_{wf},\theta)$ (mm/s), is shown in Figure 8.

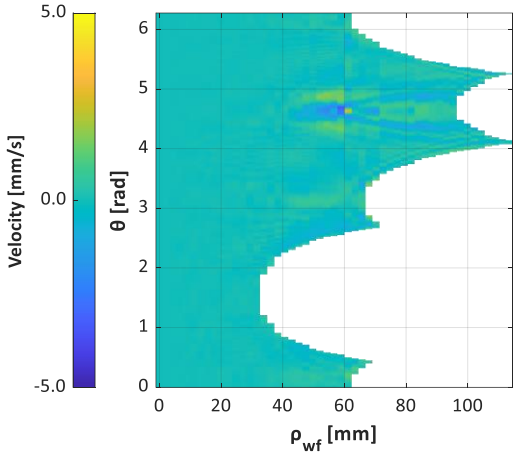

Figure 8. Filtered circumference based wavefront tracking final plot $\hat{V}(\rho_{wf},\theta)$

4. Conclusions

In this work, a new method for the detection of defects based on Lamb waves analysis has been tested on a FRP panel included a delamination with diameter approximately equal to 22 mm. To originate the vibration along the specimen a force provided by piezoelectric disk has been used. Out-of-plane velocity signals of points on the surface are acquired through a scanning laser Doppler vibrometer. The proposed technique consists on tracking the propagating antisymmetric Lamb velocity wavefront through at circumference with increasing radius at main phase velocity and centred at force origin. The final image is a plot formed by velocity amplitudes of points evaluated along the moving circumference at each polar coordinates. The application of a circumference with increasing radius as a wavefront tracking has detected the defect although the specimen is made of a typical anisotropic composite. In order to separate velocity shifts due to a non-circular propagating wavefront from the delamination effect a high-pass filter has been set. This one requires a maximum expected size of defect as input. In comparison with methods based on wavenumber imaging, our method does not allows to know the projected shape of the defect being based only on direct wave propagation. However, some geometric features, such as shape symmetry with respect to the radial direction, can be easily inferred. Lastly, more complex methods make use of at least four-dimensional matrices, making signal processing computationally more onerous as the number of scan points increases, if compared with the proposed one, which uses only the two spatial coordinates and time axes.

As a future development, a Q-switched laser source can replace the piezoelectric contact disc making the inspection system non-contact.

References

[1] Rajak D K, Pagar D D, Kumar R and Pruncu C I 2019 Recent progress of reinforcement materials: a comprehensive overview of composite materials *Journal of Materials Research and Technology* **8** 6354–74

[2] Egbo M K 2021 A fundamental review on composite materials and some of their applications in biomedical engineering *Journal of King Saud University - Engineering Sciences* **33** 557–68

[3] Parveez B, Kittur M I, Badruddin I A, Kamangar S, Hussien M and Umarfarooq M A 2022 Scientific Advancements in Composite Materials for Aircraft Applications: A Review *Polymers* **14** 5007

[4] R. A. Meyers *Encyclopedia of Physical Science and Technology 3rd edition, v. 1-18 - Robert A. Meyers - 9780122274107 - Book | Kriso.ee*
[5] Senthil K, Arockiarajan A, Palaninathan R, Santhosh B and Usha K 2013 Defects in Composite Structures: Its Effects and Prediction Methods - a Comprehensive Review *Composite Structures* **106** 139–49
[6] Wang B, Zhong S, Lee T, Fancey K and Mi J 2020 Non-destructive testing and evaluation of composite materials/structures: A state-of-the-art review *Advances in Mechanical Engineering* **12**
[7] Pant S, Laliberte J, Martinez M, Rocha B and Ancrum D 2015 Effects of composite lamina properties on fundamental Lamb wave mode dispersion characteristics *Composite Structures* **124** 236–52
[8] Lamb H 1997 On waves in an elastic plate *Proceedings of the Royal Society of London. Series A, Containing Papers of a Mathematical and Physical Character* **93** 114–28
[9] Rose J L 2014 Dispersion Principles *Ultrasonic Guided Waves in Solid Media* (Cambridge: Cambridge University Press) pp 16–35
[10] Vallée J-C, Ploix M-A, Baqué F, Cavaro M and Chaix J-F 2022 Edge and Notch Detection in a Plate Using Time Reversal Process of Leaky Lamb Waves *Applied Sciences* **12** 228
[11] Li J, Guo J, Huang H and Peng H 2021 Statistics and Analysis of Manufacturing Defects and Damage of Helicopter Composite Structures the International Council of the Aeronautical Sciences - ICAS (Shangai)
[12] STAWIARSKI A, Sanetra I and Muc A 2017 Fatigue Failure Monitoring in Composite Plate with a Circular Hole by Elastic Wave Propagation Method *DEStech Transactions on Engineering and Technology Research*
[13] Valdés S and Soutis C 2001 A Structural Health Monitoring System for Laminated Composites pp 2013–21
[14] Paget C A, Grondel S, Levin K and Delebarre C 2003 Damage assessment in composites by Lamb waves and wavelet coefficients *Smart Mater. Struct.* **12** 393
[15] Okafor A and Dutta A 2000 Structural damage detection in beams by wavelet transform *Smart Materials and Structures* **9** 906
[16] Zang C, Friswell M and Imregun M 2004 Structural Damage Detection using Independent Component Analysis *Structural Health Monitoring-an International Journal - STRUCT HEALTH MONIT* **3** 69–83
[17] Su Z, Ye L and Lu Y 2006 Guided Lamb waves for identification of damage in composite structures: A review *Journal of Sound and Vibration* **295** 753–80
[18] Yu L, Tian Z and Leckey C A C 2015 Crack imaging and quantification in aluminum plates with guided wave wavenumber analysis methods *Ultrasonics* **62** 203–12
[19] Sha G, Radzienski M, Soman R, Wandowski T, Cao M and Ostachowicz W 2020 Delamination imaging in laminated composite plates using 2D wavelet analysis of guided wavefields *Smart Mater. Struct.* **30** 015001
[20] Spytek J, Ambrozinski L and Pieczonka L 2022 Evaluation of disbonds in adhesively bonded multilayer plates through local wavenumber estimation *Journal of Sound and Vibration* **520** 116624
[21] Flynn E B, Chong S Y, Jarmer G J and Lee J-R 2013 Structural imaging through local wavenumber estimation of guided waves *NDT & E International* **59** 1–10
[22] Malone R and Sandstone Engineering 2016 *SNL API-653 In-Service Tank Inspection and Evaluation Tank ID: 981-A2-T0 (West).*
[23] Ma Z and Yu L 2021 Lamb wave imaging with actuator network for damage quantification in aluminum plate structures *Journal of Intelligent Material Systems and Structures* **32** 182–95
[24] Ibrahim R A 2017 *Handbook of Structural Life Assessment* (John Wiley & Sons)
[25] Highpass-filter signals - MATLAB highpass - MathWorks Italia